Solution Structure of Apo Cu,Zn Superoxide Dismutase: Role of Metal Ions in Protein Folding†

Lucia Banci, Ivano Bertini,* Fiorenza Cramaro, Rebecca Del Conte, and Maria Silvia Viezzoli

Department of Chemistry and Centro Risonanze Magnetiche, University of Florence, Via Luigi Sacconi 6, 50019 Sesto Fiorentino, Italy

Received February 26, 2003; Revised Manuscript Received June 13, 2003

ABSTRACT: The solution structure of the demetalated copper, zinc superoxide dismutase is obtained for the monomeric Glu133Gln/Phe50Glu/Gly51Glu mutant through NMR spectroscopy. The demetalated protein still has a well-defined tertiary structure; however, two β-strands containing two copper ligands (His46 and His48, β4) and one zinc ligand (Asp83, β5) are shortened, and the sheet formed by these strands and strands β7 and β8 moves away from the other strands of the β-barrel to form an open clam with respect to a closed conformation in the holoprotein. Furthermore, loop IV which contains three zinc ligands (His63, His71, and His80) and loop VII which contributes to the definition of the active cavity channel are severely disordered, and experience extensive mobility as it results from thorough ^{15}N relaxation measurements. These structural and mobility data, if compared with those of the copper-depleted protein and holoprotein, point out the role of each metal ion in the protein folding, leading to the final tertiary structure of the holoprotein, and provide hints for the mechanisms of metal delivery by metal chaperones.

The factors contributing to protein folding after expression are not yet completely understood. Understanding the effects produced by metal ion binding on the protein folding process and on the formation of secondary structure elements in metalloproteins is quite relevant with respect to the complete comprehension of protein stability and function. In this light, the knowledge of the structural properties of demetalated proteins is a necessary starting point and may provide hints for the interaction of the apoprotein with metal delivery proteins called metal chaperones. Within this framework, we have determined the solution structure of the apo form of copper, zinc superoxide dismutase and characterized its internal mobility. The NMR methodology is most appropriate for studying proteins which may be partially unfolded and may experience extensive mobility.

Copper, zinc superoxide dismutase (SOD)[1] is present in almost all eukaryotic cells and in a few prokaryotes (*1*). It catalyzes the dismutation of the superoxide radical to hydrogen peroxide and oxygen according to the following reactions (*2*, *3*):

$$Cu^{2+} + O_2^- \rightarrow Cu^+ + O_2$$

$$Cu^+ + O_2^- \rightarrow Cu^{2+}(O_2^{2-}) \xrightarrow{2H^+} Cu^{2+} + H_2O_2$$

The copper ion is the catalytic center. The zinc ion may play both a structural role and a role in determining the overall electrostatic field of the protein. The copper ion lies at the bottom of a wide channel that is 10 Å deep (*4*). The side chains of the residues in the active site channel create a positive electrostatic field, which plays a critical role in attracting the superoxide anion and thus determining the catalytic rates (*5*). Zinc(II) is linked to copper(II) through a histidinate bridge.

All the intracellular eukaryotic SODs are dimeric, with two identical subunits held together by hydrophobic interactions (*6*, *7*), and have a very well conserved folding topology. The quaternary structure of the dimeric enzyme determines the conformational rigidity of strategic amino acids (*8*, *9*) and strong additional stability with respect to the monomeric species (*10*). Each subunit of human SOD has 153 amino acids arranged in a Greek key β-barrel structure composed of eight antiparallel β-strands (*4*). The strands are connected by loops of various lengths, which have been numbered according to the number of the first strand they connect. Loop IV is involved in interactions between the two subunits, while loop VII (the so-called electrostatic loop) contains several charged residues which produce an electrostatic field that is suitable for guiding the superoxide anion to the copper ion (*11*−*13*). The metal ligands are located both in β-strands [His46 and His48 in β4 and His120 in β7 for the Cu(I) ion and Asp83 in β5 for the Zn(II) ion] and in loop IV [His63, -71, and -80 for the Zn(II) ion] (*4*, *6*).

Monomeric forms of the enzyme have been obtained by substituting hydrophobic residues at the subunit−subunit interface with hydrophilic residues. In particular, Phe50 and Gly51 have been substituted with two Glu residues, yielding a soluble single subunit (*14*). The enzymatic activity of this mutant (M2SOD), however, is quite reduced with respect to

† This work was supported by the European Community (Contract HPRI-CT-1999-40005), by Italian CNR (01.00238.PF49), by MIUR COFIN (ex 40%), and by Ente Cassa di Risparmio di Firenze.

* To whom correspondence should be addressed: Department of Chemistry and Centro Risonanze Magnetiche, University of Florence, Via Luigi Sacconi 6, 50019 Sesto Fiorentino, Italy. Fax: +39.055.4574271. Phone: +39.055.4574270. E-mail: bertini@cerm.unifi.it.

[1] Abbreviations: SOD, copper, zinc superoxide dismutase; Q133M2SOD, F50E/G51E/E133Q monomeric mutant of superoxide dismutase; E,Zn Q133M2SOD, copper-free (E = empty) F50E/G51E/E133Q monomeric mutant of superoxide dismutase; NMR, nuclear magnetic resonance; TPPI, time-proportional phase incrementation; ROS, reactive oxygen species.

10.1021/bi034324m CCC: $25.00
Published on Web 07/25/2003

Table 1: Acquisition Parameters for NMR Experiments Performed on Apo Q133M2SOD

	dimension of acquired data (nucleus)			spectral width (Hz)			
	t_1	t_2	t_3	F_1	F_2	F_3	ref
^{1}H−^{1}H NOESY[a]	1024 (^{1}H)	1024 (^{1}H)		25	25		*76*
^{1}H−^{15}N HSQC[b]	256 (^{15}N)	1024 (^{1}H)		2703	9254		*77*
CBCA(CO)NH[c]	256 (^{13}C)	64 (^{15}N)	2048 (^{1}H)	11627	2702	9258	*78*
HNCACB[c]	256 (^{13}C)	64 (^{15}N)	2048 (^{1}H)	11627	2702	9258	*79*
HNCO[c]	256 (^{13}C)	64 (^{15}N)	2048 (^{1}H)	9258	2702	3530	*80*
HN(CA)CO[c]	256 (^{13}C)	64 (^{15}N)	2048 (^{1}H)	9258	2702	3530	*80*
^{13}C H(C)CH-TOCSY[b]	256 (^{1}H)	48 (^{13}C)	1024 (^{1}H)	10504	11184	10504	*81*
^{13}C CC(CO)NH-TOCSY[c]	112 (^{15}N)	64 (^{15}N)	1024 (^{1}H)	80	38	15	*82*
^{13}C NOESY-HSQC[b]	320 (^{1}H)	80 (^{13}C)	1024 (^{1}H)	9259	16949	9259	*83*
^{15}N NOESY-HSQC[c]	448 (^{1}H)	40 (^{15}N)	2048 (^{1}H)	10417	3243	10417	*83*
HNHA[c]	240 (^{1}H)	32 (^{15}N)	2048 (^{1}H)	10417	2597	10417	*27*
3D HNHB[c]	128 (^{1}H)	48 (^{15}N)	2048 (^{1}H)	10417	3246	10417	*84*

[a] Data acquired on a 600 MHz spectrometer. [b] Data acquired on a 700 MHz spectrometer. [c] Data acquired on an 800 MHz spectrometer.

that of the native form, i.e., to 10% (*14*). In a monomeric variant, Glu133 has been neutralized to a Gln (*15*), to partially restore the activity. On the native protein, this mutation doubles the activity (*11*); the same occurs also on the M2SOD monomeric form (*15*) (Q133M2SOD). The global fold of monomeric SOD is essentially the same as that of a single subunit of the wild-type enzyme, characterized by the well-conserved β-barrel. Some increased disorder is observed in loop IV, located at the protein−protein interface in the native protein, which now becomes solvent-exposed (*8*). Specific structural differences, in particular, the orientation of Arg143 (*16*) in the active channel, have been found between the dimeric and monomeric forms and proposed to be responsible for the decreased catalytic activity of monomeric SOD (*8*).

This apo Q133M2SOD structure determination follows those of the fully metalated (*8*) and copper-depleted (*17*) proteins. The analysis of the structural and dynamical changes in the protein, where progressively the metal ions are removed, will allow us to determine if and to what extent the folding and the secondary structure elements are determined by the metal ions. The investigation of the monomeric species is particularly meaningful as the copper transfer between copper-depleted SOD and the copper SOD chaperone occurs *in vivo* through a monomer−monomer adduct (*18*).

MATERIALS AND METHODS

Sample Preparation. Monomeric copper, zinc Q133M2SOD was expressed in the *Escherichia coli* TOPP1 strain (Stratagene). The ^{15}N-labeled and ^{15}N- and ^{13}C-labeled proteins were obtained by growing the cells in minimal medium (M9). The samples were isolated and purified according to previously published protocols (*8*, *11*). The metal-free derivative was prepared as reported elsewhere (*2*).

The NMR samples were at a concentration of ~2 mM in 20 mM phosphate buffer (pH 5.0).

NMR Spectroscopy. The NMR experiments were recorded on Bruker Avance 800, 700, and 600 MHz spectrometers operating at 18.8, 16.4, and 14.1 T, respectively. All the experiments performed for the assignment, for the determination of the distance constraints and of the $^3J_{HNH\alpha}$ coupling constants, and for the stereospecific assignments of the Hβ protons are reported in Table 1.

A series of ^{1}H−^{15}N HSQC spectra at different temperatures, ranging from 280 to 298 K every 3 K, were acquired at 700 MHz in an effort to detect the presence of cross-peaks from amide protons which exchange with the solvent faster or at a rate comparable to their chemical shift difference with the bulk water signal. ^{1}H−^{15}N HSQC spectra were also acquired at various pHs ranging from 5 to 7.4 (physiological pH).

To detect amide hydrogen−deuterium exchange, the protein was exchanged with 100% D_2O buffer using an Amicon Micro-Ultrafiltration System. Two ^{1}H−^{15}N HSQC spectra were collected at 700 MHz, 4 h and 3 days after the buffer exchange.

All the experiments were carried out at 298 K pulsed field gradients (PFG) along the *z* axis. Quadrature detection in the indirect dimensions was performed and water suppression achieved through the WATERGATE sequence (*19*).

Data have been processed with the standard Bruker software packages (UXNMR and XWINNMR). Data analysis and assignment have been performed using the program XEASY (ETH, Zurich, Switzerland) (*20*).

^{15}N Backbone Relaxation Measurements. All NMR experiments for measuring ^{15}N relaxation rates were carried out at 298 K on a 600 Bruker Avance spectrometer. Experiments were performed with a 5 mm triple-resonance probe on samples enriched only in ^{15}N. The ^{15}N longitudinal and transversal relaxation rates, R_1 and R_2, respectively, were determined by collecting a series of ^{1}H−^{15}N HSQC spectra with a variable delay, and a phase sensitive mode, using echo−antiecho−TPPI gradient selection (*21*−*24*), was applied for water suppression. Then 2048 × 256 data points were collected using four scans for each experiment. The recycle delay was 3.0 s with an acquisition time of 136.4 ms for all the relaxation measurements. Ten experiments were carried out in an effort to measure the ^{15}N R_1 relaxation rates, with the delay ranging from 10 to 3000 ms. For the determination of the ^{15}N R_2, the CPMG pulse sequence (*23*) was used with a CPMG refocusing delay, τ_{CPMG}, of 450 μs and with the variable delays ranging from 16.96 to 305.28 ms. To monitor the contribution of exchange phenomena to the transverse relaxation rates, R_2 values were also measured as a function of the τ_{CPMG} value (*23*, *25*). Experiments were carried out with six τ_{CPMG} values from 450 to 1150 μs, with the variable delay ranging from 17 to 354 ms. Heteronuclear ^{1}H−^{15}N NOEs were measured with and without ^{1}H saturation, applied for 2.5 s (*21*). Forty-eight scans were collected for each experiment. Four spectra were recorded: two spectra with ^{1}H saturation and two without.

For all the experiments, the solvent signal was suppressed with the flip-back pulse scheme (*21*). The data were zero-filled to obtain 2048 × 512 data point matrices; a commercially available algorithm for linear prediction was used for the indirect dimension, and quadrature detection was applied using the TPPI (*22*) method.

Constraints Used in the Structure Calculations. ^{15}N and ^{13}C NOESY-HSQC cross-peaks were integrated and converted into upper distance limits for interproton distances with the program CALIBA (*26*). The calibration curves were iteratively adjusted as the structure calculations proceeded. Stereospecific assignments of diastereotopic protons were obtained using the program GLOMSA (*26*) and through the analysis of the HNHB experiment.

Backbone dihedral angle restraints ϕ were derived from $^3J_{HNH\alpha}$ coupling constants through the Karplus relationship, using the standard limits (*27*). The backbone dihedral angle ψ for residue $i-1$ was determined from the ratio of the intensity of the $H\alpha_{i-1}HN_i-H\alpha_iHN_i$ NOE cross-peaks found on the ^{15}N plane of residue i in the ^{15}N NOESY-HSQC spectrum. Ratio values of >1 are characteristic of β-strands, while values of <1 indicate a right-handed α-helix (*28*).

The presence of the disulfide bridge between Cys57 and Cys146 was checked through analysis of the ^{13}C shifts of the Cβ atoms of the cysteines. In the calculations, three upper and three lower distance limits were used to define the Cys57−Cys146 disulfide bond [between the Sγ atoms of the two Cys residues, 2.0 Å (lower) and 2.1 Å (upper), and between the Cβ atom of one Cys and the Sγ atom of the other, 3.0 Å (lower) and 3.1 Å (upper)] (*29*).

Structure calculations were performed by simulated annealing calculations within torsion angle dynamics simulations with the DYANA program (*30*). The 30 structures with the lowest target function were refined through restrained energy minimization (REM) calculations with the Sander module of the program AMBER (*31*) performed on each member of the family.

The program CORMA (*32*), which is based on relaxation matrix calculations, was used to back-calculate the NOESY cross-peaks from the calculated structure, to locate a few more cross-peaks, and to check the completeness of the assignment, which was assessed also with the AQUA program (*33*, *34*). The quality of the structure was checked through the Ramachandran analysis using the program PROCHECK-NMR (*33*).

Relaxation Data Analysis. R_1 and R_2 relaxation rates were determined by fitting the cross-peak volumes (I), measured as a function of the variable delay, to a single-exponential decay (*35*). Heteronuclear NOE values were measured as the ratio between peak volumes in spectra recorded with and without ^{1}H saturation. The heteronuclear NOE values and their errors were estimated by calculating the mean and the standard error from the available NMR data sets.

The ^{15}N relaxation rates are determined by the dipolar coupling of the ^{15}N spin with the attached proton and by the ^{15}N chemical shift anisotropy (CSA). The experimental relaxation rates were used to map the spectral density function values, $J(\omega_H)$, $J(\omega_N)$, and $J(0)$. This approach to the interpretation of ^{15}N relaxation data, proposed by Peng and Wagner (*36*), has the advantage of not requiring any assumption for the molecular tumbling. The three spectral density function values can be written as a function of the relaxation rates with the approximation of neglecting ω_N with respect to ω_H (*36*):

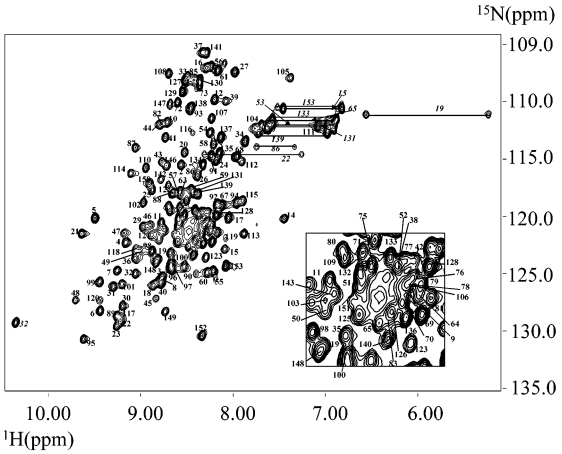

FIGURE 1: ^{1}H−^{15}N HSQC 600 MHz spectra of apo Q133M2SOD in 20 mM phosphate buffer (pH 5.0). In the inset, a close-up of the central part of the spectra is shown. The peaks due to side chain NH groups are indicated in italics.

$$J_e(0) = \frac{6R_2 - 3R_1 - \frac{18}{5}R_1(\mathrm{NOE}-1)\frac{\gamma_N}{\gamma_H}}{3d^2+4c^2}$$

$$J(\omega_N) = \frac{4R_1}{3d^2+4c^2}\left[1-\frac{7}{5}(\mathrm{NOE}-1)\frac{\gamma_N}{\gamma_H}\right]$$

$$J(\omega_H) = 0.2R_1(\mathrm{NOE}-1)\frac{4}{d^2}\frac{\gamma_N}{\gamma_H}$$

where $d = (\mu_0 h\gamma_H\gamma_N)/(8\pi^2 r_{NH}^3)$ and $c = [\omega_N(\sigma_\parallel - \sigma_\perp)]/\sqrt{3}$. $J_e(0)$ is used instead of $J(0)$ to indicate that possible contributions from conformational exchange can be operative (*36*).

^{15}N relaxation data were also analyzed in terms of the model-free formalism (*37*) through the Modelfree 4.0 program, following the reported protocol (*38*). The analysis of the overall tumbling of apo Q133M2SOD and an initial estimate of the diffusion tensor (**D**) were carried out with the program Quadric Diffusion (*39*), taking care to remove those residues having an exchange contribution to the R_2 value or exhibiting large-amplitude internal motions on a time scale longer than a few hundred picoseconds (identified from their low NOE value). Model selection in the model-free calculations was performed according to the procedure described in ref *38*, which is based on χ^2 and F statistics. The uncertainties in the model-free parameter values were estimated by Monte Carlo simulations (*38*). Fittings were performed by introducing upper limits for S^2 ($\leq$1), S_f^2 ($\leq$1), and τ_e ($<\tau_m$) and a lower limit for R_{ex} (>0). No other assumptions were used. In the last stage of the calculations, the τ_m value was optimized using the Brent algorithm together with all other model-free parameters (*38*, *40*).

R_2 data were analyzed as a function of the τ_{CPMG} length as previously reported (*41*).

RESULTS AND DISCUSSION

Resonance Assignment and Hydrogen−Deuterium Exchange. The ^{1}H−^{15}N HSQC spectra of apo Q133M2SOD (Figure 1) show a dispersion of the signals typical of a protein

which is largely in a folded state. However, several signals are present in a region of the spectra typical of unfolded polypeptides (*42*), suggesting that some parts of the protein are unstructured and experience multiple conformations. One hundred forty-three of the 147 expected $^1H-^{15}N$ backbone resonances were observed in the $^1H-^{15}N$ HSQC spectra if recorded at different temperatures. Five further signals with very low intensity were also observed. All 143 resonances were assigned, and the five weak signals were ascribed to a minor conformation.

Assignment of the ^1H_N, ^{13}C, and ^{15}N NMR resonances of the backbone nuclei was carried out using triple-resonance NMR experiments [CBCA(CO)NH, NHCACB, HN(CA)-CO, and HNCO] in addition to $^1H-^{15}N$ HSQC spectra. A total of 98.3% of the backbone resonances were assigned. It was not possible to assign the $^1H-^{15}N$ backbone resonances for Leu84, Asp124, Leu144, and Ala145, while all backbone carbonyls were assigned, with the exception of Ala123 and Leu144. The $^{13}C\alpha$ atoms were assigned for all the residues. The assignments were confirmed by the analysis of the sequential connectivities in the CC(CO)HN and ^{15}N NOESY-HSQC experiments.

The assignment of the side chain resonances was performed through the analysis of three-dimensional (3D) H(C)-CH-TOCSY and CC(CO)HN spectra together with ^{15}N NOESY-HSQC and ^{13}C NOESY-HSQC spectra. In this way, ~96% of the total proton resonances and 96% of the total ^{13}C resonances were assigned. All the nitrogen side chain resonances of Asn and Gln, with the exception of Gln133 and Gln153, were assigned. The resonance assignment is reported as Supporting Information.

The $^1H-^{15}N$ HSQC spectra were essentially invariant in the pH range of 5−7.4 (^1H shifts of <0.03 ppm), with the exception of some signals which disappear as a consequence of the increased exchange rate at pH 7.4. This indicates that we have no evidence of significant structural changes.

One hundred twenty-three amide protons, of the 143 that were detected, were still present in the $^1H-^{15}N$ HSQC spectrum acquired 4 h after exchange in 100% D_2O buffer. After 3 days, 100 peaks were still present. All these residues are located in regions with defined secondary structure. The latter are involved in an extensive H-bond network which stabilizes the β-sheet structure typical of this protein. Few exceptions are observed in strands $\beta4$ and $\beta8$, where the amide protons of Gly44 and Arg143 do exchange. Moreover, all the residues constituting strands $\beta4$ and $\beta5$ show a broadening and in some cases disappearance of the signals. Details about the exchange behavior of amide proton residues are reported in Table 1 of the Supporting Information and discussed in Comparison with E,Zn and Cu,Zn SODs.

Structure Calculation and Refinement. A total of 3083 upper distance limits (of which 2382 are meaningful), 42 ϕ and 41 ψ dihedral angle constraints were measured and used in the structural calculations, with the program DYANA (*30*). The average number of meaningful structural constraints per residue is 15.2. The number of experimental NOEs per residue, subdivided according to their class, is reported in Figure 2a. Twenty-two stereospecific assignments were obtained from the analysis of HNHB spectra and 20 from the program GLOMSA (*26*). As no information was obtained on the nature of the protonation state of the histidine ring HN groups, in the structure calculations the His residues were taken in their energetically most favored conformation, i.e., with $N_{\delta1}$ protonated. The back-calculation of the expected NOEs, carried out with the CORMA program (*32*), was performed for the ^{15}N NOESY-HSQC and ^{13}C NOESY-HSQC spectra. This analysis showed that a very small number of expected NOEs, with sizable intensity, but not present in all the conformers of the family and involving residues in the disordered regions, are missing in the experimental maps and that all the expected NOEs between assigned protons have been found.

A family of 30 conformers out of 400 with the lowest target function (average value of 1.54 ± 0.13 Å^2) was refined by performing restrained energy minimization on each member. The final family is characterized by an average rmsd value to the mean structure (for residues 3−151) of 2.25 ± 0.19 Å for the backbone and 2.83 ± 0.18 Å for the heavy atoms and an average penalty function for the distance constraints of 0.48 ± 0.05 Å^2. The rmsd drops to 0.75 ± 0.14 and 1.17 ± 0.12 Å for backbone and heavy atoms, respectively, when it is calculated without residues 45−85 and 121−144. In Figure 2b, the rmsd values, to the mean structure, per residue of the final REM family are reported. The NMR solution structure is shown in Figure 3. A statistical analysis of the family of conformers and of the average structure is reported in Table 2.

As the pH at which the structure is determined is close to the first pK_a of histidine, the calculations were also performed in the other extreme case where all the histidines are taken to be biprotonated. These calculations provided structures very close to the structures obtained with neutral histidine, consistent with the invariance of the $^1H-^{15}N$ HSQC spectra in the pH range of 5−7.4. Also, the target function yields the same value within error.

Description of the Structure. The elements of secondary structure were identified through the analysis with PROCHECK-NMR, the pattern of backbone NOEs, and the chemical shift index (CSI) (*43*) on the Cα, Cβ, Hα, and CO resonances. Eight β-strands (residues 2−7, 17−22, 29−34, 41−44, 86−89, 96−101, 116−120, and 143−151) and one α-helix (residues 133−137) were identified in the mean structure. The eight antiparallel β-strands can be divided into two regions: one with four well-defined β-strands ($\beta1-\beta3$ and $\beta6$) which form a β-sheet, with rmsd values of 0.35 ± 0.07 and 0.78 ± 0.08 Å for backbone and all heavy atoms, respectively; and the second, close in space and in sequence to the metal ion ligands, also formed by the other four β-strands ($\beta4$, $\beta5$, $\beta7$, and $\beta8$) with rmsd values of 0.59 ± 0.12 and 1.13 ± 0.18 Å for backbone and all heavy atoms, respectively. They also form a β-sheet.

Odd loops I, III, and V which connect the well-ordered β-strands ($\beta1-\beta3$ and $\beta6$) are also well-defined. Loops II and VI are less defined than odd loops I, III, and V, resembling the fully metalated protein.

Strands $\beta4$ and $\beta5$ as well as $\beta7$ and $\beta8$ are connected to each other by two loops which are the most disordered regions of the protein: loop IV (residues 45−85) and loop VII (residues 121−142). In the native protein, loop IV and the end of the two β-strands ($\beta4$ and $\beta5$) connected to it contain all the residues, except His120, coordinating both the metal ions. Loop IV, together with the electrostatic loop VII containing the α-helix, also forms the active channel of the protein which is now quite disordered. Actually, the

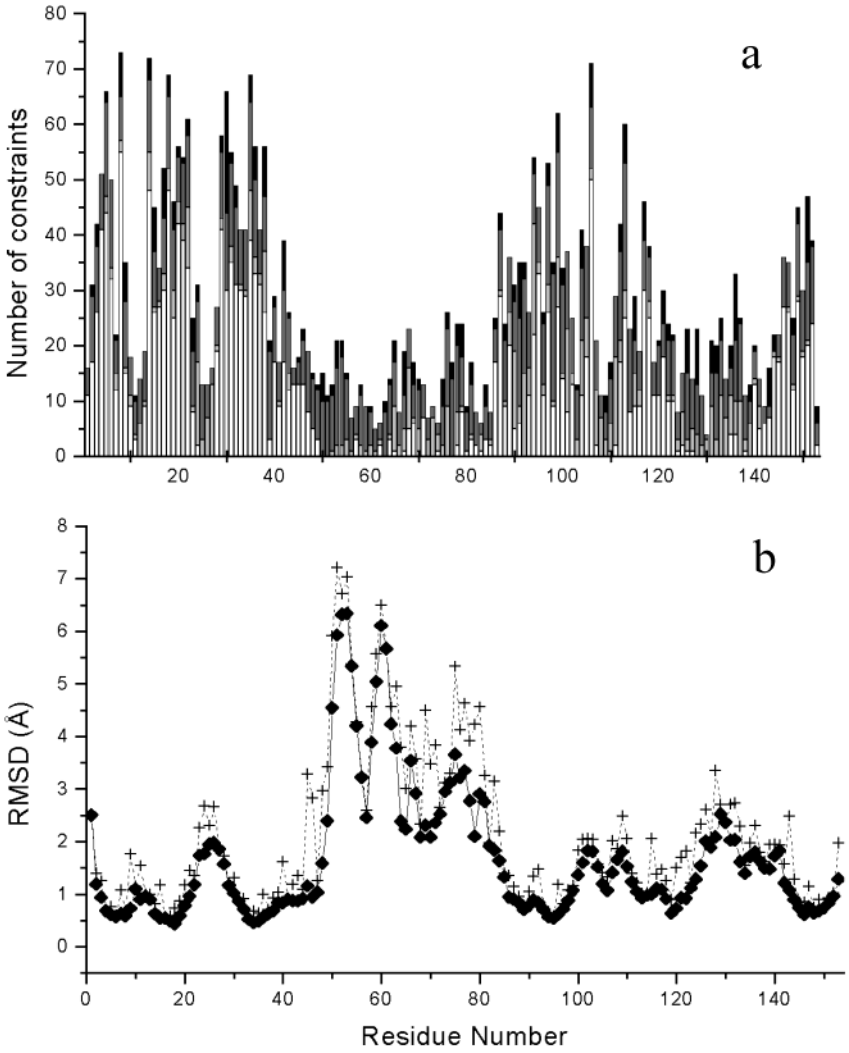

FIGURE 2: (a) Number of intraresidue (white), sequential (light gray), medium-range (gray), and long-range (black) NOEs per residue in apo Q133M2SOD. (b) Average rmsd values of backbone (◆) and heavy atoms (+) per residue with respect to the average structure of apo Q133M2SOD.

features of loop IV and loop VII suggest that these two regions are unstructured, a condition which may approach the random coil state. Random coil polypeptides are characterized by chemical shift values in small ranges typical for each residue (*42*), by an average value for $^3J_{HNH\alpha}$ of ~6.9 Hz (*44*, *45*), and by a smaller number of NOEs where the long-range NOEs are almost absent (*46*, *47*). The segments of residues 45−85 (loop IV) and 121−143 (loopVII) have chemical shift values in the ranges typical of random coil residues (Figure 1). $^3J_{HNH\alpha}$ values range between 4.5 and 7.4 Hz and between 4.0 and 7.7 Hz for loops IV and VII, respectively. Finally, very few long-range NOEs are observed for most residues in these two loops (Figure 2a). The rmsd maxima correlate closely with the smallest number of NOEs (Figure 2a) and particularly of the long-range ones. This is also in agreement with the mobility data (see below). The same pattern of NMR parameters (chemical shift values, $^3J_{HNH\alpha}$ values, and a small number of long-range NOEs) holds for those residues forming the α-helix (residues 133−137) which have a smaller number of NOEs and unusual backbone relaxation parameters (see below). The partial helical character is evidenced by $H\alpha_i-HN_{i+3}$ medium-range NOEs. A loose definition of the α-helix could be the consequence of fast conformational exchange between helix and coil conformations. The high degree of disorder of these parts of the protein is clearly a consequence of the absence of the metal ions.

Analysis of ^{15}N Relaxation Data. Reliable values of ^{15}N R_1 and R_2 and the $^1H-^{15}N$ NOE were obtained for 125 of the 143 assigned backbone NH resonances (see Figure 4). The signals of four residues (9, 46, 101, and 122) were too weak to be integrated accurately, while those of 14 residues were overlapped (8, 22, 40, 44, 50, 78, 82, 96, 97, 100, 103, 106, 121, and 143). R_1, R_2, and NOE values were relatively constant throughout the molecule with the exception of two regions, i.e., residues 52−86 (in loop IV) and 123−142 (in loop VII), where a significant increase in the R_1 values and a relevant decrease in the R_2 and NOE values were observed. Average values calculated excluding these two regions are 1.24 ± 0.09 s^{-1}, 12.6 ± 2.7 s^{-1}, and 0.68 ± 0.16 for R_1, R_2, and NOE, respectively.

The relaxation data were analyzed using the model-free formalism of Lipari and Szabo (*37*) and through the spectral density function analysis which is reported in the Supporting Information. In this analysis, for the partially unstructured segments, only an average conformation can be taken into account. An isotropic model was used for describing the rotational diffusion tensor, as no statistically significant

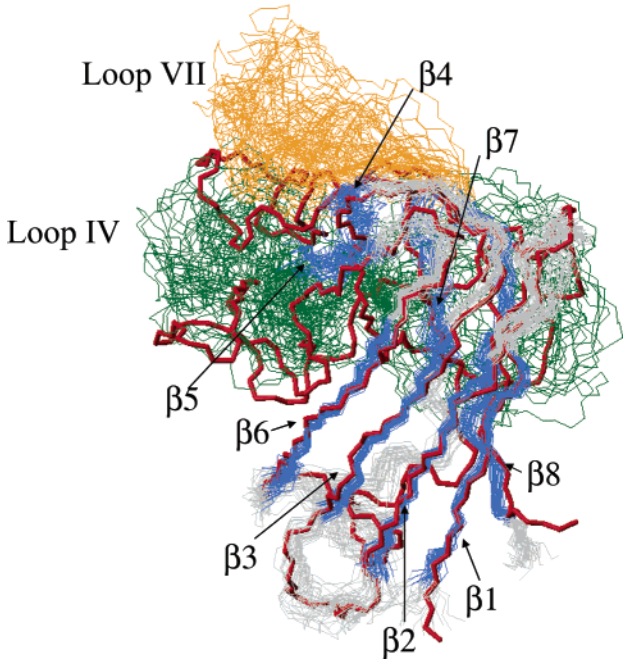

FIGURE 3: Family of 30 conformers of apo Q133M2SOD. The β-strands are shown in blue; loop IV is shown in green and loop VII in orange. As a comparison, the average structure of the fully metalated Q133M2SOD is shown in red.

improvement in the fit was obtained using an axial or fully anisotropic model. The optimized D_{iso} value is $(1.59 \pm 0.01) \times 10^7$ s^{-1}. Also in other monomeric forms, fully or partially metalated, an isotropic model for the diffusion tensor was able to correctly reproduce the relaxation data (*17*, *48*), while in the dimeric metalated form, the best fit is obtained with an axial model (*48*). The model-free parameters for the apo form are reported in Figure 4b. The relaxation rates of several residues are fitted with sizable contributions of internal motions faster than the overall molecular tumbling and for which the individual correlation times (τ_e) can been determined (Figure 4b). In the last stage of the calculations, the τ_m value was optimized, making it equal to 10.14 ± 0.29 ns which is close to the value found for the monomeric fully metalated SOD, 9.3 ± 0.10 ns (*48*), and copper-depleted SOD, 8.40 ± 0.30 ns (*17*). These experimental values are slightly higher than the values estimated from the Stokes−Einstein equation for proteins with similar molecular weights. Similar discrepancies have already been observed for other proteins (*38*, *49*−*51*). The larger τ_m value might be ascribed to the shape of the molecule, which is not spherical. Indeed, when the side chains are taken into account, the protein surface is not a smooth sphere, and this surface roughness could slow the rotation of the protein (*52*, and references therein). Furthermore, the differences in τ_m between apo SOD and the fully metalated and copper-depleted SOD may be ascribed to the increase in the size upon removal of the metal ions, as observed in the experimental structure.

From both the spectral density function and model-free analyses, it appears that two regions, residues 52−86 (in loop IV) and 123−142 (in loop VII), are characterized by striking high values of $J(\omega_H)$ and low values of $J(0)$, as well as by very low S^2 values. This behavior indicates the presence of local motions much faster than the overall protein tumbling rate. The ratio $J(\omega_N)/J(\omega_H)$, very sensitive to internal motions faster than the tumbling rate, shows a dramatic drop in its value for the residues in these two regions, consistent with the presence of fast motions (see the Supporting Information). Strikingly, but not surprisingly, the $J(\omega_N)/J(\omega_H)$ ratio parallels the number of experimental NOEs (Figure 2a). Other residues presenting some internal mobility, even if smaller than that of loops IV and VII, are Gly12 (loop I), Glu24−Gly27 (loop II), Val94 (loop V), Ile104 and Gly108−Ile112 (loop VI), Val119 (strand β7), Gly147 (strand β8), and Gln153. Most of these residues are located in loop regions.

Exchange contributions to relaxation have been observed for some residues, which have noticeably higher values of $J_e(0)$ but not higher $J(\omega_N)$, lower $J(\omega_H)$, or lower $J(\omega_N)/J(\omega_H)$ values with respect to their average values. The residues involved in exchange processes are located mainly in β-strands [Ala6 (β1), Asn19 and Glu21 (β2), Gly33 (β3), His43 (β4), Val87−Ala89 (β5), Ser98 (β6), Val118−His120 (β7), Cys146, Val148−Gly150 (β8)] and in loops [Gly10, Gly12, and Gln15 (loop I), Ile35, Lys36, and Thr39 (loop III), Val47−Glu49, Leu67, and His80 (loop IV), Asp90 (loop V), and Ala123, Asp125, and Ala140 (loop VII)]. The

Table 2: Summary of NMR Constraints, Violations, Structural Statistics, and Energetics for the Restrained Energy-Minimized Solution Structure of Apo Q133M2SOD

	REM[a] (30 structures)	⟨REM⟩[a] (mean)
rms violations per meaningful experimental distance constraint (Å)[b]		
intraresidue (421)	0.0157 ± 0.0017	0.0159
sequential (739)	0.0136 ± 0.0011	0.0143
medium-range (257)[c]	0.0137 ± 0.0029	0.0109
long-range (965)	0.0112 ± 0.0013	0.0110
total (2382)	0.0132 ± 0.0008	0.0130
rms violations per experimental dihedral angle constraint (deg)[b]		
ϕ (42)	7.05 ± 2.11	7.3
ψ (41)	2.69 ± 0.11	2.0
average no. of violations per structure lower than 0.3 Å		
intraresidue	13.6 ± 2.8	10
sequential	22.9 ± 3.1	27
medium-range	8.9 ± 2.7	6
long-range	17.5 ± 2.8	15
total	62.9 ± 5.0	58
ϕ	4.2 ± 1.7	4
ψ	0.8 ± 0.7	1
average no. of NOE violations larger than 0.3 Å	0	0
structural analysis[d]		
% of residues in most favorable regions	69.9	80.4
% of residues in allowed regions	26.7	17.4
% of residues in generously allowed regions	3.0	2.2
% of residues in disallowed regions	0.4	0
experimental restraint analysis[e]		
completeness of experimentally observed NOEs up to 4 Å cutoff distance (%)	75	62
completeness of experimentally observed NOEs up to 5 Å cutoff distance (%)	54	44

[a] REM represents the energy-minimized family of 30 structures, and ⟨REM⟩ is the energy-minimized mean structure obtained from the coordinates of the individual REM structures. [b] The number of meaningful experimental constraints for each class is reported in parentheses. [c] Medium-range distance constraints are those between residues i and $i + 2$, i and $i + 3$, i and $i + 4$, and i and $i + 5$. [d] As it results from the Ramachandran plot analysis on the secondary structure elements. [e] As it results from the AQUA analysis (*33*) over all the residues of the protein (*34*).

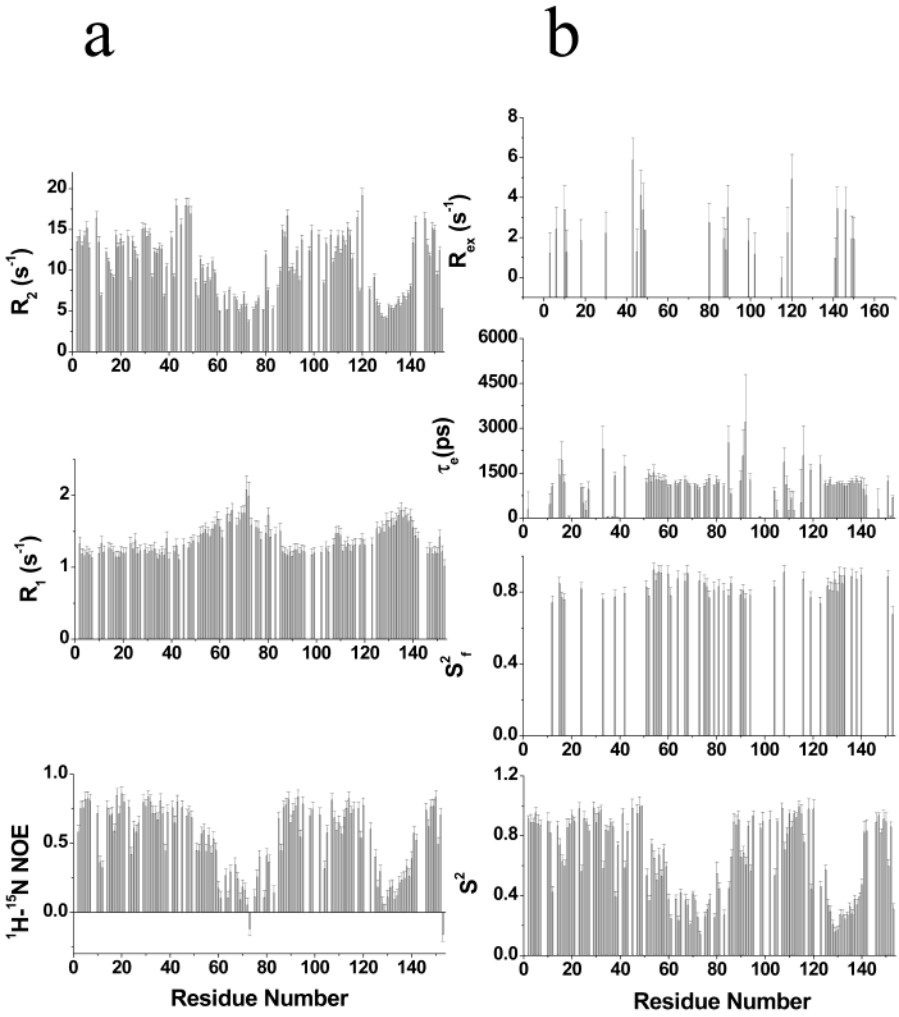

FIGURE 4: ^{15}N relaxation parameters (a) and model-free parameters (b) vs residue number for apo Q133M2SOD.

presence of exchange contributions to transverse relaxation was also independently evaluated through R_2 measurements as a function of the τ_{CPMG} length which also provide the correlation time for the exchange process (see Materials and Methods). The latter data are reported in Table 6 of the Supporting Information. Fourteen of the above residues, mostly located in odd loops, show a dependence of R_2 on the τ_{CPMG} length which indicates that the exchange process occurs with a rate in the range of 70−120 μs (limits determined by the experimental conditions).

Three of the β-strands (β4, β5, and β7) involved in exchange processes are connected to loops IV and VII, i.e., those regions experiencing the highest rmsd values and most extensive sub-nanosecond mobility, while the other two β-strands (β6 and β8) are antiparallel to the former three β-strands. The occurrence of these "slow" motions involving β-strands may be related to "breathing" motions of the β-barrel. Similar motions have also been observed for other proteins with a similar β-barrel fold (*48*, *50*, *53*). It is also relevant that two residues which bind the copper ion in native SOD and whose backbone HN group can be detected (His48 and His120) and one Zn ligand (His80) experience an exchange contribution in the apo form.

Comparison with E,Zn and Cu,Zn SODs. The ^{1}H and ^{15}N chemical shift differences and the weighted average chemical shift differences $\Delta_{average}$(HN) (*54*) of backbone resonances among the fully metalated Q133M2SOD, the copper-depleted E,Zn Q133M2SOD, and the apo Q133M2SOD forms are reported in Figure 5. The distribution of chemical shift differences is clearly not homogeneous over the entire sequence but rather reflects significant structural changes in loops IV and VII and in the β4, β5, and β7 strands for the apo form with respect to both fully metalated and copper-depleted proteins. These regions are those characterized by a small number of NOEs, high rmsd values, and high mobility in the apo form. Some β-strands are shortened. Particularly sizable is the reduction of strand β4 which stretches from residue 41 to 48 in the native and copper depleted forms and from residue 41 to 44 in the apo form. Consequently, the length of loop IV increases significantly, from residues 49−82 in the native protein to residues 45−85 in the apo form. The shortening of strand β4 moves two copper ligands (His46 and His48) in a loop, whereas they are in the β-strand in both metalated forms. Several residues of the β4 strand also experience a striking difference in the hydrogen−deuterium exchange with respect to the fully metalated (*55*) and copper-depleted (*17*) forms. Indeed, in the apo form, the amide HN signals of three of the four residues forming the β4 strand disappear after 4 days, while in the holoprotein and in the copper-depleted form, all the amide resonances of the β4 strand do not exchange with the bulk solvent within 5 days.

The observation that the fully metalated and copper-depleted forms are very similar to each other but different

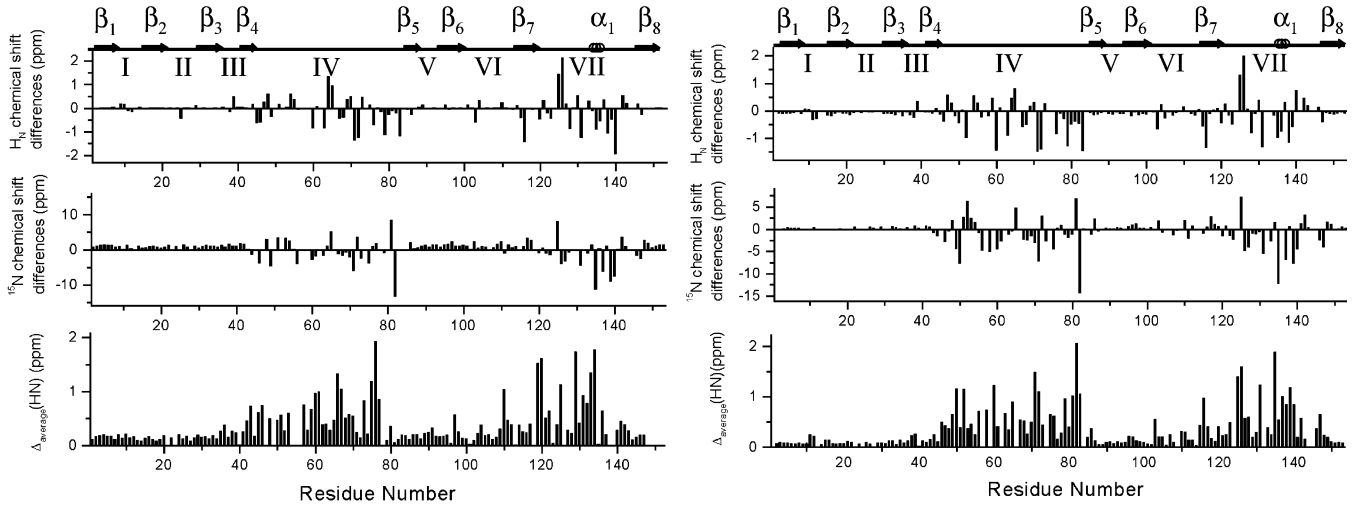

FIGURE 5: Chemical shift differences between Cu,Zn Q133M2SOD and apo Q133M2SOD (left) and between E,Zn Q133M2SOD and apo Q133M2SOD (right) for the backbone amide proton (top) and backbone nitrogen (middle) and the weighted average chemical shift differences $\Delta_{average}$(HN) (*16*) (bottom). The secondary structure of the apo form is also reported at the top. Roman numerals denote the loops.

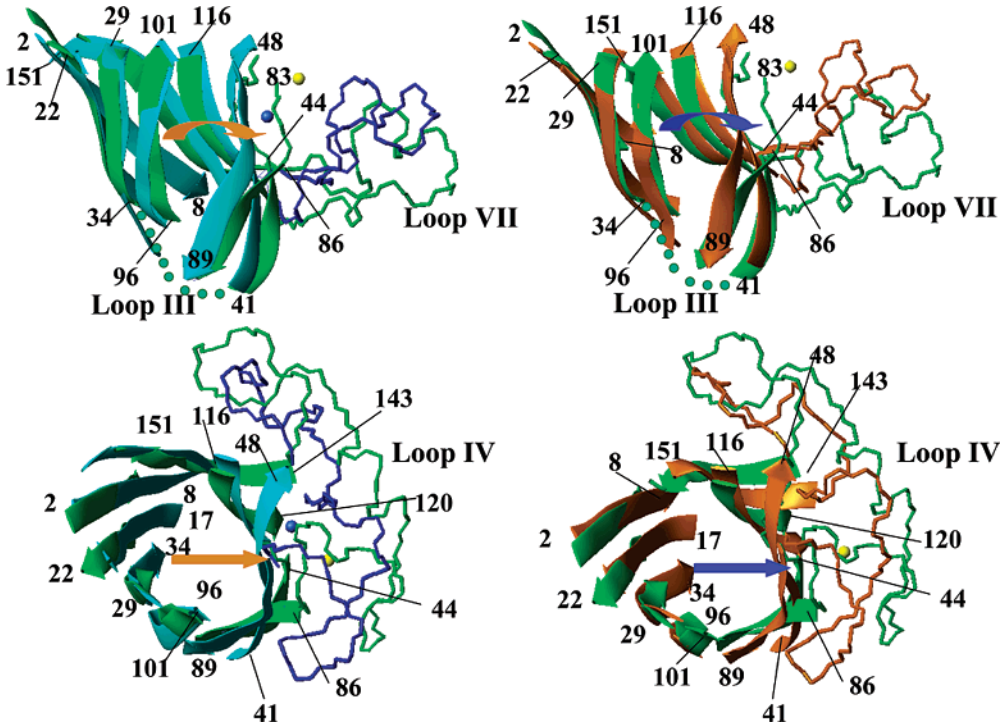

FIGURE 6: Comparison between the mean structures of the apo Q133M2SOD (green) and Cu,Zn Q133M2SOD (cyan) (left) and between apo Q133M2SOD (green) and E,Zn Q133M2SOD (orange) (right). The β-strand and loops IV and VII with a schematic representation of loop III (•••) are shown. The yellow sphere represents the Zn ion and the blue sphere the copper ion. All the structures were fitted to the β-barrel of apo Q133M2SOD.

from the apo form suggests that Zn has a quite relevant role in determining the fold and the full development of secondary structure elements. In Figure 6, the apo structure is compared with those of the metalated proteins. It appears that the β-sheet formed by strands β4, β5, β7, and β8 and loops IV and VII moves further away from the other β-sheet in the apo form with respect to the distances in the other structures, thus producing an increased width of the upper part of the active channel. In this movement (Figure 6), loops III and V act as a hinge which defines the relative position and orientation of the β-sheets. These conformational changes make the zinc site solvent-exposed in the apo form. The relevant structural role of these loops in determining the subunit fold was already pointed out in the analysis of ALS-related point mutation distribution (*56*). Their structural role relies significantly on an extensive network of H-bonds between these two loops and residues in the β-barrel as observed in the dimeric wild-type protein (*16*).

The mobility data indicate an unstructured state for loop IV in the apoprotein, the first part of which shows also some disorder in the fully metalated monomeric form. In the dimeric native protein, the first part of loop IV is well-ordered and is located at the interface between the two subunits which is completely solvent-exposed in the monomeric forms. The second segment loses its defined conformation as a consequence of the lack of both metal ions. Multiple conformations are also present, in the apoprotein, for the electrostatic loop VII (residues 121−142), where some relevant H-bonds are

Table 3: Conserved H-Bonds between Residues of Loop VII, Loop IV, and the Active Site in Some SOD Solution Structures

H-bond	apo Q133M2SOD[a]	E,Zn Q133M2SOD[b]	Q133M2SOD[c]	dimeric SOD[d]
Asn86 $HN_{\delta 2}$···CO 124	absent	absent	present	present
118 HN···CO 46	absent	present	present	present
119 HN···CO 145	absent	present	present	present
120 HN···CO 44	absent	present	present	present

[a] Structure presented here. [b] Taken from ref *17*. [c] Taken from ref *8*. [d] Taken from ref *16*.

lost. On the contrary, these H-bonds are present in the fully metalated monomeric and dimeric SODs (Table 3), and most of them also in the copper-depleted form.

Effects of Metal Ion Binding. Despite the absence of metal ions, the protein is well-ordered in one of the two four-stranded β-sheets, whereas the other four-stranded β-sheet is reduced in size in comparison with the zinc-loaded and the copper- and zinc-loaded proteins, although still well organized. In the apoprotein, the two β-sheets look like an opened clam, whereas they form a Greek key β-barrel in the other species. Loop IV, which is involved in the dimerization of the native protein, is longer in the apo species, quite disordered, and flexible. Loop VII, which is involved in defining the active cavity, is also extremely disordered. From the comparison of the available structures of SOD with different metal contents, it appears that the binding of zinc has dramatic structuring effects; it organizes all the β-strands with the full length as found in the native state and induces the complete tertiary structure and the optimal conformation of the electrostatic loop VII. Metal binding, even only zinc, also induces a sizable reduction in the internal mobility.

The availability of these structures allows us to propose some hypotheses for the metal uptake processes. While the metal chaperone responsible for copper binding to SOD, the CCS protein, is known and has been characterized (*18*, *57*), no protein has been yet found which carries zinc to the apoprotein. The order of the metal uptake is not known *in vivo*; however, there is strong evidence that zinc binds before copper (*1*, *58*−*60*). The role of zinc in SOD has been matter of discussion for decades (*58*). It has been suggested that zinc binding preforms the copper site (*61*) and enhances its affinity for copper (*62*). Furthermore, once zinc binds, there is a decrease in disorder and mobility. The structure presented here clearly shows that zinc has a major structural role in the organization of the entire structure and in particular of the copper binding site.

Biological Implications. One-electron reduction of oxygen and the following partial reduction lead to the production of reactive oxygen species (ROS) such as superoxide radicals, hydrogen peroxide, and hydroxyl radicals which can damage DNA, lipids, and proteins (*63*−*66*). Superoxide dismutase, which catalyzes the disproportionation of superoxide to hydrogen peroxide and water, represents a most important defense against ROS (*2*, *67*). In eukaryotes, 90% of the total superoxide dismutation activity is due to homodimeric copper, zinc SOD which is located in the cytosol (*68*). *In vivo*, the SOD protein reaches its active form through interaction with CCS, a dimeric copper chaperone protein which delivers copper ions to SOD. The metal transfer step has been proposed to occur within a heterodimeric complex comprising one monomer of CCS and one monomer of SOD (*18*, *69*−*71*), the formation of which is facilitated by the presence of zinc (*69*). A model involving interactions between the two homodimers has also been proposed (*57*). Therefore, the characterization of a monomeric apo form of SOD is quite relevant with respect to understanding the processes of metal incorporation. In this study, the monomeric protein obtained through site-directed mutagenesis on the dimeric interface has been characterized before the binding of any metal ion, from both the structural and dynamic points of view. In the apoprotein, the two β-sheets that form the typical SOD Greek key β-barrel in the zinc-bound protein and the copper- and zinc-bound protein look like an open clam, with one of the two sheets reduced in size. The movement of one of the two β-sheets with respect to the other increases the width of the upper part of the active channel, thus making the putative zinc site solvent-exposed and ready to bind zinc. Two loops, one involved in the dimerization of the native protein (loop IV) and the other, the so-called electrostatic loop, or loop VII, involved in defining the active cavity, are quite disordered and flexible. Once zinc binds, the protein undertakes the final folding, leaving only the copper binding site disordered and somewhat open (*57*, *69*−*72*). Despite the process of zinc binding *in vivo* being unknown as no protein has been recognized as a putative chaperone of this process, the structure of the apoprotein might be suitable for the complex formation with the zinc chaperone, and once the zinc is transferred, a conformational trigger occurs which allows the zinc protein to interact with the copper chaperone CCS (*18*, *69*).

The role of zinc in SOD is that of providing a positive charge and a structural stability to the holoenzyme (*59*, *73*, *74*) and to be involved in the catalytic mechanism through the histidine−histidinato 63 link (*75*). The comparison between the structure of the apoprotein and the zinc-bound protein suggests a further role of zinc, i.e., that of providing the correct structure for the interaction with CCS.

SUPPORTING INFORMATION AVAILABLE

Resonance assignments, experimental NOE intensities, ϕ torsion angle constraints, ψ torsion angle constraints, stereospecific assignments of diastereotopic pairs, backbone amide nitrogens showing a dependence of R_2 on the τ_{CPMG} lengths, spectral density functions, and ratios of the spectral functions $J(\omega_N)/J(\omega_H)$ versus the residue number for apo Q133M2SOD at 298 K in 20 mM phosphate buffer (pH 5.0). This material is available free of charge via the Internet at http://pubs.acs.org.

REFERENCES

1. Bertini, I., Mangani, S., and Viezzoli, M. S. (1998) in *Advanced Inorganic Chemistry* (Sykes, A. G., Ed.) pp 127−250, Academic Press, San Diego.
2. McCord, J. M., and Fridovich, I. (1969) Superoxide dismutase. Enzymic function for erythrocuprein, *J. Biol. Chem. 244*, 6049−6055.

3. Fee, J. A., and Gaber, B. P. (1972) Anion binding to bovine erythrocyte superoxide dismutase. Evidence for multiple binding sites with qualitatively different properties, *J. Biol. Chem. 247*, 60−65.
4. Tainer, J. A., Getzoff, E. D., Richardson, J. S., and Richardson, D. C. (1983) Structure and Mechanism of Copper, Zinc Superoxide Dismutase, *Nature 306*, 284−287.
5. Banci, L., Bertini, I., Luchinat, C., and Hallewell, R. A. (1988) An investigation of superoxide dismutase Lys-143, Ile-143, and Glu-143 mutants: Cu_2Co_2SOD derivatives, *J. Am. Chem. Soc. 110*, 3629−3633.
6. Tainer, J. A., Getzoff, E. D., Beem, K. M., Richardson, J. S., and Richardson, D. C. (1982) Determination and Analysis of 2 Å Structure of Copper Zinc Superoxide Dismutase, *J. Mol. Biol. 160*, 181−217.
7. Parge, H. E., Getzoff, E. D., Scandella, C. S., Hallewell, R. A., and Tainer, J. A. (1986) Crystallographic characterization of recombinant human CuZn superoxide dismutase, *J. Biol. Chem. 261*, 16215−16218.
8. Banci, L., Benedetto, M., Bertini, I., Del Conte, R., Piccioli, M., and Viezzoli, M. S. (1998) Solution structure of reduced monomeric Q133M2 Copper, Zinc Superoxide Dismutase. Why is SOD a dimeric enzyme? *Biochemistry 37*, 11780−11791.
9. Ferraroni, M., Rypniewski, W., Wilson, K. S., Viezzoli, M. S., Banci, L., Bertini, I., and Mangani, S. (1999) The crystal structure of the monomeric human SOD mutant F50/G51E/E133Q at atomic resolution. The enzyme mechanism revisited, *J. Mol. Biol. 288*, 413−426.
10. Bozzi, M., Battistoni, A., Sette, M., Melino, S., Rotilio, G., and Paci, M. (2001) Unfolding and inactivation of monomeric superoxide dismutase from *E. coli* by SDS, *Int. J. Biol. Macromol. 29*, 99−105.
11. Getzoff, E. D., Cabelli, D. E., Fisher, C. L., Parge, H. E., Viezzoli, M. S., Banci, L., and Hallewell, R. A. (1992) Faster Superoxide Dismutase Mutants designed by Enhancing Electrostatic Guidance, *Nature 358*, 347−351.
12. Banci, L., Cabelli, D. E., Getzoff, E. D., Hallewell, R. A., and Viezzoli, M. S. (1993) An Essential Role for the Conserved Glu-133 in the Anion Interaction with Superoxide Dismutase, *J. Inorg. Biochem. 50*, 89−100.
13. Fisher, C. L., Cabelli, D. E., Tainer, J. A., Hallewell, R. A., and Getzoff, E. D. (1994) The role of Arginine 143 in the Electrostatic and Mechanism of Cu,Zn Superoxide Dismutase: Computational and Experimental Evaluation of Site-directed Mutants, *Proteins: Struct., Funct., Genet. 19*, 24−34.
14. Bertini, I., Piccioli, M., Viezzoli, M. S., Chiu, C. Y., and Mullenbach, G. T. (1994) A spectroscopic characterization of a monomeric analog of copper−zinc superoxide dismutase, *Eur. J. Biophys. 23*, 167−176.
15. Banci, L., Bertini, I., Chiu, C. Y., Mullenbach, G. T., and Viezzoli, M. S. (1995) Synthesis and characterization of a monomeric mutein of Cu/Zn superoxide dismutase with partially reconstituted enzymatic activity, *Eur. J. Biochem. 234*, 855−860.
16. Banci, L., Bertini, I., Cramaro, F., Del Conte, R., and Viezzoli, M. S. (2002) The solution structure of reduced dimeric copper zinc SOD: the structural effects of dimerization, *Eur. J. Biochem. 269*, 1905−1915.
17. Banci, L., Bertini, I., Cantini, F., D'Onofrio, M., and Viezzoli, M. S. (2002) Structure and dynamics of copper-free SOD: The protein before binding copper, *Protein Sci. 11*, 2479−2492.
18. Lamb, A. L., Torres, A. S., O'Halloran, T. V., and Rosenzweig, A. C. (2001) Heterodimeric structure of superoxide dismutase in complex with its metallochaperone, *Nat. Struct. Biol. 8*, 751−755.
19. Piotto, M., Saudek, V., and Sklenar, V. (1992) Gradient-tailored excitation for single quantum NMR spectroscopy of aqueous solutions, *J. Biomol. NMR 2*, 661−666.
20. Eccles, C., Güntert, P., Billeter, M., and Wüthrich, K. (1991) Efficient analysis of protein 2D NMR spectra using the software package EASY, *J. Biomol. NMR 1*, 111−130.
21. Grzesiek, S., and Bax, A. (1993) The importance of not saturating H_2O in protein NMR. Application to sensitivity enhancement and NOE measurements, *J. Am. Chem. Soc. 115*, 12593−12594.
22. Marion, D., and Wüthrich, K. (1983) Application of phase sensitive correlated spectroscopy (COSY) for measurements of proton−proton spin−spin coupling constants in proteins, *Biochem. Biophys. Res. Commun. 113*, 967−974.
23. Kay, L. E., Nicholson, L. K., Delaglio, F., Bax, A., and Torchia, D. A. (1992) Pulse sequences for removal of the effects of cross correlation between dipolar and chemical-shift anisotropy relaxation mechanisms on the measurement of heteronuclear T_1 and T_2 values in proteins, *J. Magn. Reson. 97*, 359−375.
24. Kay, L. E., Torchia, D. A., and Bax, A. (1989) Backbone dynamics of proteins as studied by ^{15}N inverse detected heteronuclear NMR spectroscopy: application to staphylococcal nuclease, *Biochemistry 28*, 8972−8979.
25. Peng, J. W., and Wagner, G. (1994) Investigation of protein motions via relaxation measurements, *Methods Enzymol. 239*, 563−596.
26. Güntert, P., Braun, W., and Wüthrich, K. (1991) Efficient computation of three-dimensional protein structures in solution from nuclear magnetic resonance data using the program DIANA and the supporting programs CALIBA, HABAS and GLOMSA, *J. Mol. Biol. 217*, 517−530.
27. Vuister, G. W., and Bax, A. (1993) Quantitative J Correlation: A New Approach for Measuring Homonuclear Three-Bond $J(H^NH^\alpha)$ Coupling Constants in ^{15}N Enriched Proteins, *J. Am. Chem. Soc. 115*, 7772−7777.
28. Gagné, R. R., Tsuda, S., Li, M. X., Chandra, M., Smillie, L. B., and Sykes, B. D. (1994) Quantification of the calcium-induced secondary structural changes in the regulatory domain of troponin-C, *Protein Sci. 3*, 1961−1974.
29. Williamson, M. P., Havel, T. F., and Wüthrich, K. (1985) Solution Conformation of Proteinase Inhibitor IIA from Bull Seminal Plasma by ^{1}H Nuclear Magnetic Resonance and Distance Geometry, *J. Mol. Biol. 185*, 295−315.
30. Güntert, P., Mumenthaler, C., and Wüthrich, K. (1997) Torsion Angle Dynamics for NMR Structure Calculation with the New Program DYANA, *J. Mol. Biol. 273*, 283−298.
31. Pearlman, D. A., Case, D. A., Caldwell, J. W., Ross, W. S., Cheatham, T. E., Ferguson, D. M., Seibel, G. L., Singh, U. C., Weiner, P. K., and Kollman, P. A. (1997) *AMBER*, version 5.0, University of California, San Francisco.
32. Borgias, B., Thomas, P. D., and James, T. L. (1989) *COmplete Relaxation Matrix Analysis (CORMA)*, version 5.0, University of California, San Francisco.
33. Laskowski, R. A., Rullmann, J. A. C., MacArthur, M. W., Kaptein, R., and Thornton, J. M. (1996) AQUA and PROCHECK-NMR: Programs for checking the quality of protein structures solved by NMR, *J. Biomol. NMR 8*, 477−486.
34. Laskowski, R. A., MacArthur, M. W., and Thornton, J. M. (1998) Validation of protein models derived from experiment, *Curr. Opin. Struct. Biol. 8*, 631−639.
35. Marquardt, D. W. (1963) An algorithm for least-squares estimation of nonlinear parameters, *J. Soc. Ind. Appl. Math. 11*, 431−441.
36. Peng, J. W., and Wagner, G. (1992) Mapping of spectral density function using heteronuclear NMR relaxation measurements, *J. Magn. Reson. 98*, 308−332.
37. Lipari, G., and Szabo, A. (1982) Model-free approach to the interpretation of nuclear magnetic resonance relaxation in macromolecules. 2. Analysis of experimental results, *J. Am. Chem. Soc. 104*, 4559−4570.
38. Mandel, M. A., Akke, M., and Palmer, A. G., III (1995) Backbone dynamics of *Escherichia coli* ribonuclease HI: correlations with structure and function in an active enzyme, *J. Mol. Biol. 246*, 144−163.
39. Lee, L. K., Rance, M., Chazin, W. J., and Palmer, A. G., III (1997) Rotational diffusion anisotropy of proteins from simultaneous analysis of ^{15}N and ^{13}C alpha nuclear spin relaxation, *J. Biomol. NMR 9*, 287−298.
40. Lipari, G., and Szabo, A. (1982) Model-free approach to the interpretation of nuclear magnetic resonance relaxation in macromolecules. 1. Theory and range of validity, *J. Am. Chem. Soc. 104*, 4546−4559.
41. Orekhov, V. Y., Pervushin, K. V., and Arseniev, A. S. (1994) Backbone dynamics of (1−71) bacterioopsin studied by two-dimensional ^{1}H-^{15}N NMR spectroscopy, *Eur. J. Biochem. 219*, 887−896.
42. Wishart, D. S., Bigam, C. G., Holm, A., Hodges, R. S., and Sykes, B. D. (1995) ^{1}H, ^{13}C and ^{15}N random coil NMR chemical shifts of the common amino acids. I. Investigations of nearest-neighbor effects, *J. Biomol. NMR 5*, 67−81.
43. Wishart, D. S., and Sykes, B. D. (1994) The ^{13}C chemical shift index: a simple method for the identification of protein secondary structure using ^{13}C chemical shift data, *J. Biomol. NMR 4*, 171−180.
44. Schwalbe, H., Fiebig, K. M., Buck, M., Jones, J. A., Grimshaw, S. B., Spencer, A., Glaser, S. J., Smith, L. J., and Dobson, C. M. (1997) Structural and dynamical properties of a denatured protein.

Heteronuclear 3D NMR experiments and theoretical simulations of lysozyme in 8 M urea, *Biochemistry 36*, 8977−8991.
45. Frank, M. K., Clore, G. M., and Gronenborn, A. M. (1995) Structural and dynamic characterization of the urea denatured state of the immunoglobin binding domain of streptococcal protein G by multidimensional heteronuclear NMR spectroscopy, *Protein Sci. 4*, 2605−2615.
46. Brutscher, B., Brüschweiler, R., and Ernst, R. R. (1997) Backbone dynamics and structural characterization of the partially folded A state of ubiquitin by ^{1}H, ^{13}C, ^{15}N nuclear magnetic resonance spectroscopy, *Biochemistry 36*, 13043−13053.
47. Kuloglu, E. S., McCaslin, D. R., Kitabwalla, M., Pauza, C. D., Markley, J. L., and Volkman, B. F. (2001) Monomeric solution structure of the prototypical "C" chemokine lymphotactin, *Biochemistry 40*, 12486−12496.
48. Banci, L., Bertini, I., Cramaro, F., Del Conte, R., Rosato, A., and Viezzoli, M. S. (2000) Backbone Dynamics of Human Cu, Zn Superoxide Dismustase and of its Monomeric F50/EG51E/E133Q Mutant: The Influence of Dimerization on Mobility and Function, *Biochemistry 39*, 9108−9118.
49. Powers, R., Clore, G. M., Stahl, S. J., Wingfield, P. T., and Gronenborn, A. M. (1992) Analysis of the backbone dynamics of the ribonuclease H domain of the human immunodeficiency virus reverse transcriptase using ^{15}N relaxation measurements, *Biochemistry 31*, 9150−9157.
50. Redfield, C., Boyd, J., Smith, L. J., Smith, R., and Dobson, C. M. (1992) Loop mobility in a four-helix-bundle protein: nitrogen-15 NMR relaxation measurements on human interleukin-4, *Biochemistry 31*, 10431−10437.
51. Kelley, J. J. I., Caputo, T. M., Eaton, S. F., Laue, T. M., and Bushweller, J. H. (1997) Comparison of backbone dynamics of reduced and oxidized *Escherichia coli* glutaredoxin-1 using ^{15}N NMR relaxation measurements, *Biochemistry 36*, 5029−5044.
52. Van-Quynh, A., Willson, S., and Bryant, R. G. (2003) Protein reorientation and bound water molecules measured by ^{1}H magnetic spin−lattice relaxation, *Biophys. J. 84*, 558−563.
53. Cheng, J. W., Lepre, C. A., Chambers, S. P., Fulghum, J. R., Thomson, J. A., and Moore, J. M. (1993) ^{15}N NMR relaxation studies of the FK506 binding protein: backbone dynamics of the uncomplexed receptor, *Biochemistry 32*, 9000−9010.
54. Garrett, D. S., Seok, Y. J., Liao, D. I., Peterkofsky, A., Gronenborn, A. M., and Clore, G. M. (1997) N-Terminal domain of enzyme I of the *Escherichia coli* phosphoenolpyruvate:sugar phosphotransferase system by multidimensional NMR, *Biochemistry 36*, 2517−2530.
55. Banci, L., Benedetto, M., Bertini, I., Del Conte, R., Piccioli, M., Richert, T., and Viezzoli, M. S. (1997) Assignment of backbone NMR resonances and secondary structural elements of a reduced monomeric mutant of copper/zinc superoxide dismutase, *Magn. Reson. Chem. 35*, 845−853.
56. Deng, H. X., Hentati, A., Tainer, J. A., Lqbal, Z., Cyabyab, A., Hang, W.-Y., Getzoff, E. D., Hu, P., Herzfeldt, B., Roos, R. P., Warner, C., Deng, G., Soriano, E., Smyth, C., Parge, H. E., Ahmed, A., Roses, A. D., Hallewell, R. A., Pericak-Vance, M. A., and Siddique, T. (1993) Amyotrophic lateral sclerosis and structural defects in Cu,Zn superoxide dismutase, *Science 261*, 1047−1051.
57. Hall, L. T., Sanchez, R. J., Holloway, S. P., Zhu, H., Stine, J. E., Lyons, T. J., Demeler, B., Schirf, V., Hansen, J. C., Nersissian, A. M., Valentine, J. S., and Hart, P. J. (2000) X-ray crystallographic and analytical ultracentrifugation analyses of truncated and full-length yeast copper chaperones for SOD (LYS7): a dimer-dimer model of LYS7-SOD association and copper delivery, *Biochemistry 39*, 3611−3623.
58. Beem, K. M., Rich, W. E., and Rajagopalan, K. V. (1974) Total Reconstitution of Copper-Zinc Superoxide Dismutase, *J. Biol. Chem. 249*, 7298−7305.
59. Lippard, S. J., Burger, A. R., Ugurbil, K., Pantoliano, M. W., and Valentine, J. S. (1977) Nuclear magnetic resonance and chemical modification studies of bovine erythrocyte superoxide dismutase: evidence for zinc-promoted organization of the active site structure, *Biochemistry 16*, 1136−1141.
60. Pantoliano, M. W., Valentine, J. S., Burger, A. R., and Lippard, S. J. (1982) A pH-dependent superoxide dismutase activity for zinc-free bovine erythrocuprein. Reexamination of the role of zinc in the holoprotein, *J. Inorg. Biochem. 17*, 325−341.
61. Cass, A. E., Hill, H. A. O., Bannister, J. V., and Bannister, W. H. (1979) Zinc(II) binding to apo-(bovine erythrocyte superoxide dismutase), *Biochem. J. 177*, 477.
62. Roe, J. A., Peoples, R., Scholler, D. M., and Valentine, J. S. (1990) Silver-binding properties of bovine cuprozinc superoxide dismutase and the overall stability of selected metal-ion derivatives, *J. Am. Chem. Soc. 112*, 1538−1545.
63. Fridovich, I. (1978) The biology of oxygen radicals, *Science 201*, 875−879.
64. Fridovich, I. (1983) Superoxide radical: an endogenous toxicant, *Annu. Rev. Pharmacol. Toxicol. 23*, 239−257.
65. Halliwell, B., Gutteridge, J. M. C., and Blake, D. (1985) Metal ions and oxygen radical reactions in human inflammatory joint disease, *Philos. Trans. R. Soc. London, Ser. B 311*, 659−671.
66. Halliwell, B., and Gutteridge, J. M. (1984) Oxygen toxicity, oxygen radicals, transition metals and disease, *Biochem. J. 219*, 1−14.
67. Fridovich, I. (1986) Superoxide dismutase, *Adv. Enzymol. Relat. Areas Mol. Biol. 58*, 61−97.
68. Crapo, J. D., Oury, T., Rabouille, C., Slot, J. W., and Chang, L. Y. (1992) Copper,zinc superoxide dismutase is primarily a cytosolic protein in human cells, *Proc. Natl. Acad. Sci. U.S.A. 89*, 10405−10409.
69. Lamb, A. L., Torres, A. S., O'Halloran, T. V., and Rosenzweig, A. C. (2000) Heterodimer formation between superoxide dismutase and its copper chaperone, *Biochemistry 39*, 14720−14727.
70. Rae, T. D., Torres, A. S., Pufahl, R. A., and O'Halloran, T. V. (2001) Mechanism of Cu,Zn-superoxide dismutase activation by the human metallochaperone hCCS, *J. Biol. Chem. 276*, 5166−5176.
71. Torres, A. S., Petri, V., Rae, T. D., and O'Halloran, T. V. (2001) Copper-stabilized heterodimer of the yCCS metallochaperone and its target superoxide dismutase, *J. Biol. Chem. 276*, 38410−38426.
72. Schmidt, P. J., Rae, T. D., Pufahl, R. A., Hamma, T., Strain, J., O'Halloran, T. V., and Culotta, V. C. (1999) Multiple protein domains contribute to the action of the copper chaperone for superoxide dismutase, *J. Biol. Chem. 274*, 23719−23725.
73. Rotilio, G., Calabrese, L., Bossa, F., Barra, D., Finazzi Agró, A., and Mondovì, B. (1972) Properties of the Apoprotein and Role of Copper and Zinc in Protein Conformation and Enzyme Activity of Bovine Superoxide Dismutase, *Biochemistry 11*, 2182−2187.
74. Pantoliano, M. W., Valentine, J. S., Mammone, R. J., and Scholler, D. M. (1982) pH dependence of metal ion binding to the native zinc site of bovine erythrocuprein (superoxide dismutase), *J. Am. Chem. Soc. 104*, 1717−1723.
75. Strothkamp, K. G., and Lippard, S. J. (1982) Chemistry of the Imidazolate-Bridged Bimetallic Center in the Cu-Zn Superoxide Dismutase and Its Model Compounds, *Acc. Chem. Res. 15*, 318−326.
76. Macura, S., Wüthrich, K., and Ernst, R. R. (1982) The relevance of *J* cross-peaks in two-dimensional NOE experiments of macromolecules, *J. Magn. Reson. 47*, 351−357.
77. Sklenar, V., Piotto, M., Leppik, R., and Saudek, V. (1993) Gradient-tailored water suppression for ^{1}H-^{15}N HSQC experiments optimized to retain full sensitivity, *J. Magn. Reson., Ser. A 102*, 241−245.
78. Grzesiek, S., and Bax, A. (1992) Correlating backbone amide and side chain resonances in larger proteins by multiple relayed triple resonance NMR, *J. Am. Chem. Soc. 114*, 6291−6293.
79. Grzesiek, S., and Bax, A. (1992) Improved 3D Triple-Resonance NMR Techniques Applied to a 31 kDa Protein, *J. Magn. Reson. 96*, 432−440.
80. Kay, L. E., Ikura, M., Tschudin, R., and Bax, A. (1990) Three-Dimensional Triple-Resonance NMR Spectroscopy of Isotopically Enriched Proteins, *J. Magn. Reson. 89*, 496−514.
81. Kay, L. E., Xu, G. Y., Singer, A. U., Muhandiram, D. R., and Forman-Kay, J. D. (1993) A gradient-enhanced HCCH-TOCSY experiment for recording side-chains ^{1}H and ^{13}C correlations in H_2O samples of proteins, *J. Magn. Reson., Ser. B 101*, 333−337.
82. Gardner, K. H., Konrat, R., Rosen, M. K., and Kay, L. E. (1996) An (H)C(CO)NH-TOCSY pulse scheme for sequential assignment of protonated methyl groups in otherwise deuterated ^{15}N, ^{13}C-labeled proteins, *J. Biomol. NMR 8*, 351−356.
83. Wider, G., Neri, D., Otting, G., and Wüthrich, K. (1989) A Heteronuclear Three-Dimensional NMR Experiment for Measurements of Small Heteronuclear Coupling Constants in Biological Macromolecules, *J. Magn. Reson. 85*, 426−431.
84. Archer, S. J., Ikura, M., Torchia, D. A., and Bax, A. (1991) An alternative 3D NMR technique for correlation backbone ^{15}N with side chain Hβ resonances in larger proteins, *J. Magn. Reson. 95*, 636−641.

BI034324M